Journal of Alloys and Compounds 1012 (2025) 178500

Contents lists available at ScienceDirect

Journal of Alloys and Compounds

journal homepage: www.elsevier.com/locate/jalcom

Microstructural modification in an Al-Mg-Si (6082) alloy with high Fe content using inoculation and/or high-intensity ultrasonication

M.H. Khan [a,*], A. Das [b], T.I. Khan [c], Z. Li [a], H.R. Kotadia [a,d,**]

[a] WMG, The University of Warwick, Coventry CV4 7AL, UK
[b] Faculty of Science and Engineering, Swansea University, Bay Campus, Swansea SA1 8EN, UK
[c] School of Engineering, The University of Bradford, Bradford BD7 1DP, UK
[d] School of Engineering, Liverpool John Moores University, Liverpool L3 3AF, UK

ARTICLE INFO

Keywords:
Aluminium alloys
Iron containing intermetallics
Solidification
Ultrasonication
Cavitation
Inoculation
Microstructure refinement

ABSTRACT

In this study, the effects of solute Ti, chemical grain refiner (GR), and ultrasonication (UT) on the solidification behaviour and microstructure of a 6xxx (Al-1.0Mg-1.0Si) alloy with 1.0 wt% Fe impurity were examined. Primary-Al grains and eutectic Fe-intermetallic compounds (Fe-IMCs), predominantly α – Al_8Fe_2Si/β – $Al_9Fe_2Si_2$, were identified as the major phases through thermodynamic prediction and microstructural observation. The results show that UT treatment produced the finest and most uniform microstructure, improving both grain refinement and Fe-IMC distribution, particularly compared to chemical methods. UT, when combined with GR, enhanced TiB_2 dispersion and improved the nucleation of both Al grains and Fe-IMCs, leading to better refinement of the Fe-IMCs. Chemical inoculation also showed some effect, but UT consistently displayed finer, more uniform microstructures, and less aggregation of TiB_2 particles. Although TiB_2 particles appear to help nucleation of Fe-IMCs, refinement and distribution of the IMCs was primarily contributed by the size and distribution of intergranular liquid pockets, and consequently, the refinement of the Al-grain structure. Overall, the study highlights that UT, in combination with GR and TiB_2, significantly improves the microstructure and controls Fe-IMC formation in high Fe 6xxx alloys, offering a promising approach for refining Al-Mg-Si alloys with high Fe content.

1. Introduction

Aluminium (Al) alloys are important structural materials and second only to steel as the most used metal. Desirable properties including excellent specific strength, low density, good crash resistance, high formability and resistance to corrosion, make Al alloys attractive to the transportation sector [1,2]. Despite these advantages, accumulation of unwanted tramp elements such as iron (Fe) and silicon (Si), which builds up during recycling, is highly detrimental to mechanical performance of Al-alloys. If Fe concentration increases above the industrial limit of 0.2 wt%, Fe-rich intermetallics (Fe-IMCs) form as Fe solid solubility in Al is limited to 0.05 wt%. The formation of Fe-IMCs in wrought Al-alloys deteriorate mechanical properties and formability [3]. It is known that Fe cannot be removed entirely from Al-alloys, however, some methods are being explored to minimise the detrimental effect of Fe-IMCs. The four most common methods include: (i) addition of trace elements (Mn, Cr, Cu, Zr, etc), which modifies the acicular β – $Al_9Fe_2Si_2$ to less detrimental Chinese script α – Al_8Fe_2Si; [4–6] (ii) addition of solute elements such as titanium (Ti) or grain refiners such as TiB_2 to effectively refine the microstructure and improve mechanical performance; [7,8] (iii) use of physical fields such as ultrasonication (UT); electromagnetic stirring or intensive shearing to refine and disperse Fe-IMCs and (iv) manipulating solidification parameters such as cooling rates to alter the microstructure [9–12].

Among these methods, the two most effective ways of achieving microstructural refinement is the use of chemical inoculation or a physically induced techniques such as UT. The addition of TiB_2, through master alloy, acts as a nucleating agent promoting the formation of numerous grains during solidification. Our previous investigation [2] identified that refining microstructure through chemical inoculation directly influenced Fe-IMC size, shape and phase selection. In particular, Al-grain refinement was observed to effectively reduce the size of the

* Corresponding author.
** Corresponding author at: WMG, The University of Warwick, Coventry CV4 7AL, UK.
E-mail addresses: Mir-Hamza.H.Khan@warwick.ac.uk (M.H. Khan), h.r.kotadia@ljmu.ac.uk (H.R. Kotadia).

https://doi.org/10.1016/j.jallcom.2025.178500
Received 22 October 2024; Received in revised form 14 December 2024; Accepted 4 January 2025
Available online 5 January 2025

Fe-IMCs due to confined growth space in the smaller intergranular liquid pockets. The exact mechanism through which residual TiB_2 segregate at the solid/liquid (S/L) interface and nucleate Fe-IMCs requires investigation. Lui et al. [13] proposed that convective forces during solidification causes residual TiB_2 particles to segregate into the S/L interface. However, there has been no clarification on the effect of grain structures and its influence on the segregation of TiB_2 particles in the interdendritic regions.

Previous investigation has found that besides refining grains, UT has better control in reducing the size of Fe-IMCs in comparison to chemical inoculation [9]. It has been suggested that microstructural refinement by UT is achieved through cavitation in the melt under ultrasound irradiation [11,14–17]. Grain refining by UT is separated into two mechanisms: (i) dendritic fragmentation via cavitation and ultrasonic streaming; (ii) cavitation (collapsing of gas bubbles) enhanced nucleation. Despite numerous studies by [16,18–20], that have attempted to explain UT refinement, there is no systematic study on the overall effect on Fe-IMC evolution under higher residual Fe content (1.0 wt%) in the industrially important Al-Mg-Si alloys (e.g., 6082). Previous studies have focused on the Al-Si, Al-Cu or Al-Mg based alloys, where it is still unclear how effective UT combined with solute elements is in refining primary-Al and Fe-IMCs. In addition, studies have shown that UT coupled with Sn, Mn, Cu, Bi, additions led to marginal refinement of the microstructures. It is worth noting that some investigations conducted by [11,21–23] highlighted that effectiveness of UT treatment depends not only on UT parameters such as frequency, power, and fluid flow, but also on the chemical nature of the Al melt such as the growth restriction factor (GRF) of the solute present and chemical inoculation (Al-5Ti-1B addition). These factors are important and should be considered when conducting a comprehensive study. Therefore, in this study the effects of small addition of high GRF solute (Ti additions of up to 0.03 wt%), chemical grain refiner (Al-5Ti-1B). and UT, in isolation or in conjunction, has been investigated on the development of Fe-IMCs in an Al-Mg-Si alloy containing 1.0 wt% Fe.

2. Experimental procedure

2.1. Alloy preparation

The Al-Mg-Si (6082) alloy was prepared from commercially pure Al (99.87 wt%) with the addition of appropriate hardeners (e.g. Al-20Mg, Al-20Si, Al-10Fe) by melting in a clay graphite crucible in an electric furnace. The Al melt was homogenised for at least one hours at 750 °C with intermittent stirring to chemically homogenise the melt. For experiments involving chemical grain refinement, a pre-measured quantity of Al-5Ti-1B (GR) master alloy was added to the Al melt with 1 gm/kg ratio (industry limit) 5 minutes prior to casting. Compositions of the different alloy samples were verified through optical emission spectroscopy (Foundry Master Pro), see Table 1.

2.2. Casting experiments

The Al melt was taken out of the furnace at 750 °C and degassed with argon (~3 minutes) until reaching temperatures of 700 °C. The melt was then cast in a graphite crucible under UT by placing an ultrasonic horn 20 mm into the melt as shown in Fig. 1. The setup consisted of a 500 Watt and 20 kHz ultrasonic generator, with the Ti–6Al–4 V radiator of 25 mm diameter, with a radius of 2.5 mm generating vibration at an amplitude of 8 μm. It is important to note that the ultrasound horn was preheated to 450 °C by submerging it into a batch of Al melt to minimise any chill effect. The six sonicated alloys were (1) 1.0 wt% Fe (reference); (2) 1.0 wt% Fe + Ti (solute), (3) 1.0 wt% Fe + GR (TiB_2); (4) 1.0 wt% Fe + UT (ultrasonication); (5) 1.0 wt% Fe+ Ti + UT; (6) 1.0 wt% Fe + GR + UT, see Table 1.

Table 1
Chemical composition (in wt%) for all alloys investigated.

Alloy designation	Mg	Si	Fe	Ti	Al	GR (Al-5Ti-1B)
6082/1.0 Fe Reference	0.995	1.03	1.1	-	Balance	
1.0Fe+Ti	0.991	1.02	1.1	0.03	Balance	
1.0Fe+GR	0.997	1.01	1.12	-	Balance	√
1.0Fe+UT	0.986	1.01	1.11	-	Balance	
1.0Fe+Ti+UT	0.997	1.0	1.0	0.03	Balance	
1.0Fe+GR+UT	0.997	1.01	1.1	-	Balance	√

2.3. Thermal analysis and computational thermodynamics prediction

Primary-Al and Fe-IMC solidification was investigated via cooling curves measured using a K-type thermocouple connected to a multi-channel data logger (Micro-Measurements System 8000). Thermal analysis was conducted using a NETZSCH STA449 F3 Differential Scanning Calorimeter (DSC) to confirm phase nucleation temperatures. For DSC analysis, 20 mg sample was placed inside an alumina crucible and heated at 1 °C /s between 100 C - 750 °C. The cooling curves and DSC analysis were repeated twice to ensure the accuracy of results. The results from the thermal analysis were compared with Thermo-Calc predictions (Aluminium alloy database: TCAL 4: Mobile v4.0 and MOBAL3) to identify and correlate phase nucleation temperatures.

2.4. Microstructural characterisation and analysis

Standard metallographic preparation was performed using Buehler procedure, which included sectioning and mounting the samples in conductive Bakelite, followed by grinding with SiC paper (up to 400 grit [P800]) and polishing with 0.06 μm colloidal silica. Samples were subsequently cleaned using isopropyl in an ultrasonic bath for 10 seconds. Anodizing with Barkers reagent (7 ml 48 % HBF_4, 93 ml H_2O) for approximately 70 seconds at 20 V was performed to reveal the primary-Al grain structure under polarised light microscopy. A JEOL 7800F Scanning Electron Microscope (SEM) equipped with Electron Backscatter Diffraction (EBSD) and Energy Dispersive X-ray Spectroscopy (EDS) detectors (oxford) was employed to examine the microstructure using an accelerating voltage of 15 kV and 10 mm working distance. When identifying the Fe-IMCs, the Kikuchi patterns were indexed at low median average deviation (MAD) values of 0.45–0.70. To chemically map the TiB_2 particles, EDS was used with an accelerating voltage of 15 kV, a current of 10 nA and dwell time of 250 ms to allow for a high-count rate and high-resolution chemical maps. To observe the detailed structures of the Fe-IMCs, the samples were deep etched for using 37 % HCl for 90 s to investigate the morphology of the IMCs.

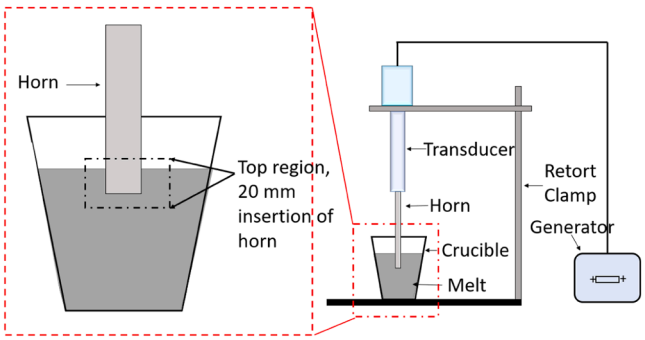

Fig. 1. Schematic diagram illustrating the setup of the ultrasonication device.

3. Results

3.1. Primary-Al microstructures

Microstructural characterisation was carried out in three regions of the ingots: from the top (close to horn), middle and bottom of the ingot (close to graphite crucible wall), see Fig. 2 (A–C). The results showed that the reference 6082 alloy with 1.0 wt% Fe (called the 1.0Fe alloy henceforth) had the largest average grain size of 2718 ± 157 μm in region 'A'. Region 'B' had an average grain size of 2636 ± 131 μm and region 'C' showed a value of 2601 ± 133 μm. There is a refinement in the grain size following the addition of Ti (0.03 wt%) to the reference alloy, henceforth referred to as 1.0Fe+Ti alloy, in comparison to the reference sample and the average grain sizes were 1210 ± 119 μm, 992 ± 97 μm and 831 ± 92 μm in regions 'A', 'B' and 'C', respectively. Grain refinement was significant with the addition of Al-5Ti-1B grain refiner to the reference alloy (henceforth called the 1.0Fe+GR alloy) throughout the ingot, and it was noted that grain size was smallest at the bottom of region 'C' (539 ± 70 μm) in comparison to region 'A' (713 ± 57 μm) and 'B' (671 ± 69 μm). The microstructures presented in Fig. 2 for the 1.0Fe+GR alloy shows fine-equiaxed dendritic grains throughout the ingot.

Considerable grain refinement was observed in the reference alloy under ultrasonication treatment (1.0Fe+UT) as coarse dendritic structures is replaced with fine-equiaxed grain morphology as shown in Fig. 2. The effect of UT on grain refinement was most prominent in region 'A' (317 ± 39 μm) relative to region 'B' (with 377 ± 52 μm) or region 'C' (with 416 ± 54 μm). This was thought to be due to region 'A'

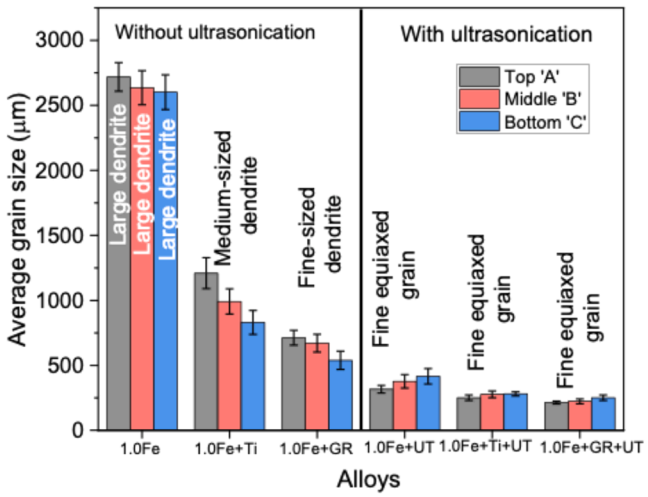

Fig. 3. The measured average Al grain size and its morphology for all alloys from various regions of the ingots.

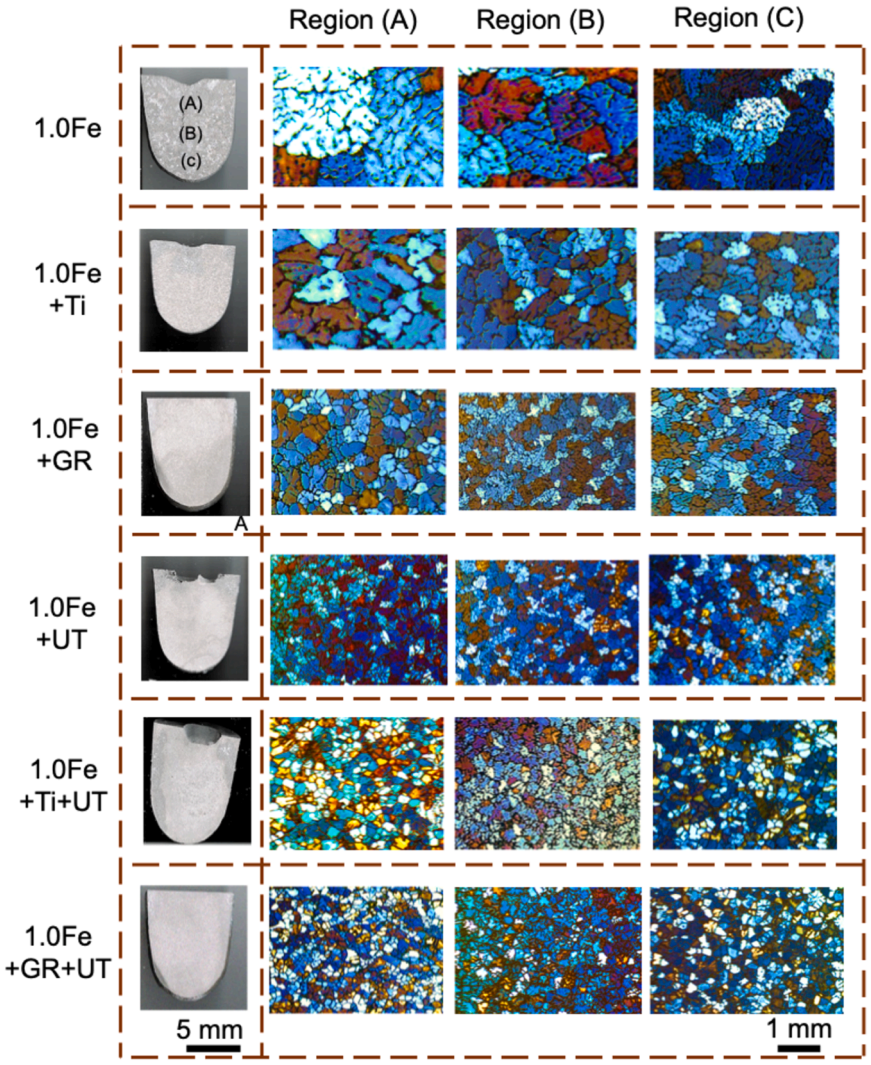

Fig. 2. Microstructures from various regions (as defined in top left) of the Al-Mg-Si-Fe ingots demonstrating the primary-Al grain structure.

being the nearest to the submerged UT horn with most effective refinement occurring closest to the horn [10]. Similar results were observed for ultrasonicated alloys with Ti addition (1.0Fe+Ti+UT) in regions 'A' to 'C' (251 ± 29 μm to 281 ± 16 μm) and alloys with grain refiner addition (1.0Fe+GR+UT) in Region 'A' to 'C' (214 ± 11 μm to 251 ± 21 μm) with the grains being polygonal in shape. The difference in grain size could be attributed to 1.0Fe+GR+UT having Al-5Ti-1B addition, compared to the addition of Ti solute in the 1.0Fe+Ti+UT samples. The highest grain refinement was observed in 1.0Fe+GR+UT as the combination of UT and inoculation by TiB_2 was more effective in grain refinement as opposed to just chemical inoculation through TiB_2 in alloy 1.0Fe+GR.

3.2. Thermal analysis

The cooling curves for all samples, with and without UT, are shown in Fig. 4. The nucleation temperature of primary-Al, as measured from the cooling curves, exhibited variations among the alloys and is summarised in Table 2. The difference in the nucleation undercooling for the primary-Al phase is dictated by the effect of solutes, chemical inoculation and UT. There is a noticeable reduction in the undercooling for primary-Al nucleation in samples with Ti, GR, and UT as compared to the reference alloy. The increase in primary-Al nucleation temperature from 644.1 °C in the reference alloy (1.0Fe) to 646.1 °C in the 1.0Fe+Ti alloy suggests nucleation enhancement from the solute Ti addition. Addition of GR shows higher nucleation potency with a measured Al nucleation temperature of 647.1 °C in the 1.0Fe+GR alloy. This is expected as the TiB_2 particles in the grain refiner are well-known heterogeneous nucleant for Al while solute Ti predominantly aids Al nucleation through constitutional undercooling. However, the lowest undercooling (or the highest nucleation temperature) was noticed in the alloys solidified under UT that also demonstrated lower recalescence. The primary-Al nucleation temperatures measured for the 1.0Fe+UT, 1.0Fe+Ti+UT and 1.0Fe+GR+UT alloys are 647.5 °C, 647.9 °C and 648.9 °C, respectively. This indicates better Al-nucleation enhancement under UT compared to the chemical routes and that UT can further enhance the nucleation efficiency of Ti solute or GR when used in conjunction.

3.3. Solidification microstructure of Fe-IMCs

The Fe-IMCs formed in the as-cast microstructure, in regions 'A' and 'C' across all six alloys, can be seen in Fig. 5 with Fig. 6(a and b) presenting the measured average Fe-IMC size. The regions 'A' and 'C' are of interest when analysing the Fe-IMCs because they represent the areas solidifying at different times at different cooling rates and thus influence the nucleation and growth of Fe-IMCs. Additionally, the effect of settling of heavier IMCs would influence the largest variation in microstructure between the region's 'A' and 'C'.

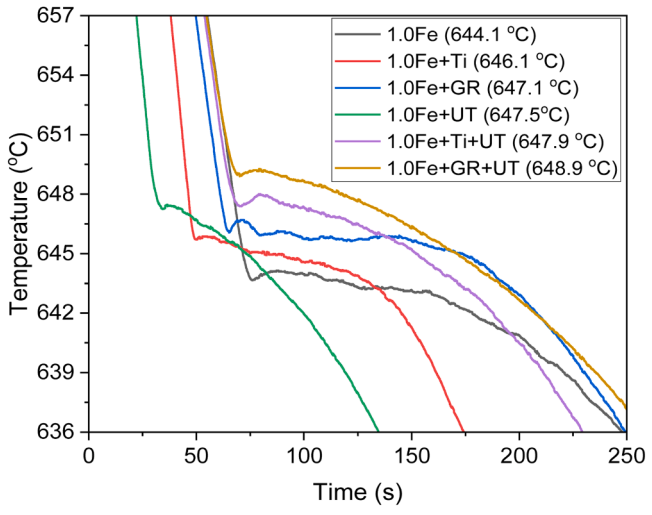

Fig. 4. Cooling curves measuring the primary-Al nucleation temperature for all alloys during solidification.

The as-cast microstructures, presented in Fig. 5, show prevalence of the $\beta - Al_9Fe_2Si_2$ phase resembling needle like structures in 2-dimensional form and faceted plates in 3-dimension. The $\alpha - Al_8Fe_2Si$ phase also seems to be present in all six alloys, resembling Chinese script morphology. However, the $\beta - Al_9Fe_2Si_2$ phase is the most notable in the as-cast structures.

Based on the quantitative results, it appears that the reference alloy 1.0Fe has the course $\beta - Al_9Fe_2Si_2$ IMC with average length measuring 463 ± 26.3 μm in region 'A' and 440 ± 17.1 μm in region 'C'. For the 1.0Fe+Ti alloy, there is a decrease in the Fe-IMC length compared to the reference alloy with a measured average length varying from 371± 21.7 μm to 332 ± 14.4 μm between regions 'A' to 'C'. It was also noted that the addition of Ti does not affect the morphological transformation of $\beta - Al_9Fe_2Si_2$ phase. For the inoculated alloy 1.0Fe+GR, there is further reduction in the $\beta - Al_9Fe_2Si_2$ IMC size varying from 229 ±15.2 μm to 212 ± 15.9 μm between regions 'A' and 'C'. The difference in the Fe-IMCs average length between the alloys 1.0Fe, 1.0Fe+Ti and 1.0Fe+GR show similar trends as with the primary-Al grain size and is most likely related to the effect of grain refinement on the eutectic areas where the IMCs form and grow. The solidification conditions for all the alloys studied are expected to be identical. Alloys; 1.0Fe, 1.0Fe+Ti and 1.0Fe+GR, have slightly larger Fe-IMCs, in region 'A' where cooling rate is slower and intergranular eutectic areas are larger as opposed to region 'C'. Conversely, smaller Fe-IMCs form near the bottom of the ingot (region 'C') with increased heat loss from the melt in contact with the crucible wall and the smaller intergranular eutectic areas.

The experimental results also show a significant overall reduction in the $\beta - Al_9Fe_2Si_2$ IMC length in all regions for all concerned alloys under ultrasonication. The average b-length measured was from 130 ± 8.7 μm to 171 ± 9.1 μm between regions 'A' to 'C' in alloy 1.0Fe+UT, Average b-length measured between regions 'A' to 'C' for 1.0Fe+Ti+UT (114 ± 8.8 μm to 142 ± 7.4 μm) and 1.0Fe+GR+UT (107 ± 6.7 μm to 127 ± 5.5 μm) showed similar overall trend. Interestingly, the UT samples show progressive IMC refinement from the bottom to the top of the samples in contrast with samples without UT where the IMC refinement was progressive from the top to the bottom as shown in Fig. 5. This replicates the trends observed with primary-Al grain refinement in the samples as discussed in Section 3.1. The Fe-IMC were observed to be the finest in alloy 1.0Fe+GR+UT although the variation in average IMC size is marginal between different ultrasonicated alloys as shown in Fig. 6(a) unlike the non-sonicated alloys where the addition of Ti and GR involved significant alteration in the IMC size. It appears that UT has a stronger influence on the IMC refinement compared to chemical means.

Fe-IMCs area fraction for all six alloys processed under different conditions were calculated and presented in Fig. 6(b). It is important to note that any increase in the area fraction refers to the percentage of the field of view covered by the Fe-IMCs and does not indicate an increase in Fe wt% as the Fe content was fixed at ~1.0 wt% for all alloys. The chemical nature of the Fe-IMCs along with their size, morphology, and distribution affects the overall area fraction under the different processing conditions.

The Fe-IMC area faction shows an increase with the addition of Ti and GR to the base alloy. The measured values in the region's 'A' and 'C', are 3.9 % and 3.6 % for the reference alloy 1.0Fe, 4.2 % and 4.1 % for alloy 1.0Fe+Ti, and 4.4 % and 4.6 % for alloy 1.0Fe+GR, respectively.

Under ultrasonication, the Fe-IMC area fraction increased for all the alloys with values measured in the region's 'A' and 'C', being 5.4 % and 5.1 % for 1.0Fe+UT, 5.7 % and 5.3 % for 1.0Fe+Ti+UT, and 6.2 % and 5.9 % for 1.0Fe+GR+UT, respectively. For the alloys under UT, region 'A' consistently showed highest area fraction of Fe-IMCs in all alloys. This is consistent with the observation of finer and better dispersion of

Table 2
Comparison of nucleation temperatures for the primary-Al and Fe-IMC phases for 1.0Fe, 1.0Fe+Ti and 1.0Fe+GR alloys.

Alloy	Phase transformation/nucleation temperature (°C)						
	Primary − Al			$Al_{13}Fe_4/\alpha - Al_8Fe_2Si$		$\beta - Al_9Fe_2Si_2$	
	Thermo-Calc	DSC	Cooling Curve	Thermo-Calc	DSC	Thermo-Calc	DSC
1.0Fe	645	650	644	636	633	596	572
1.0Fe+Ti	647	650	646	638	634	594	576
1.0Fe+GR	-	650	647	-	635	-	585

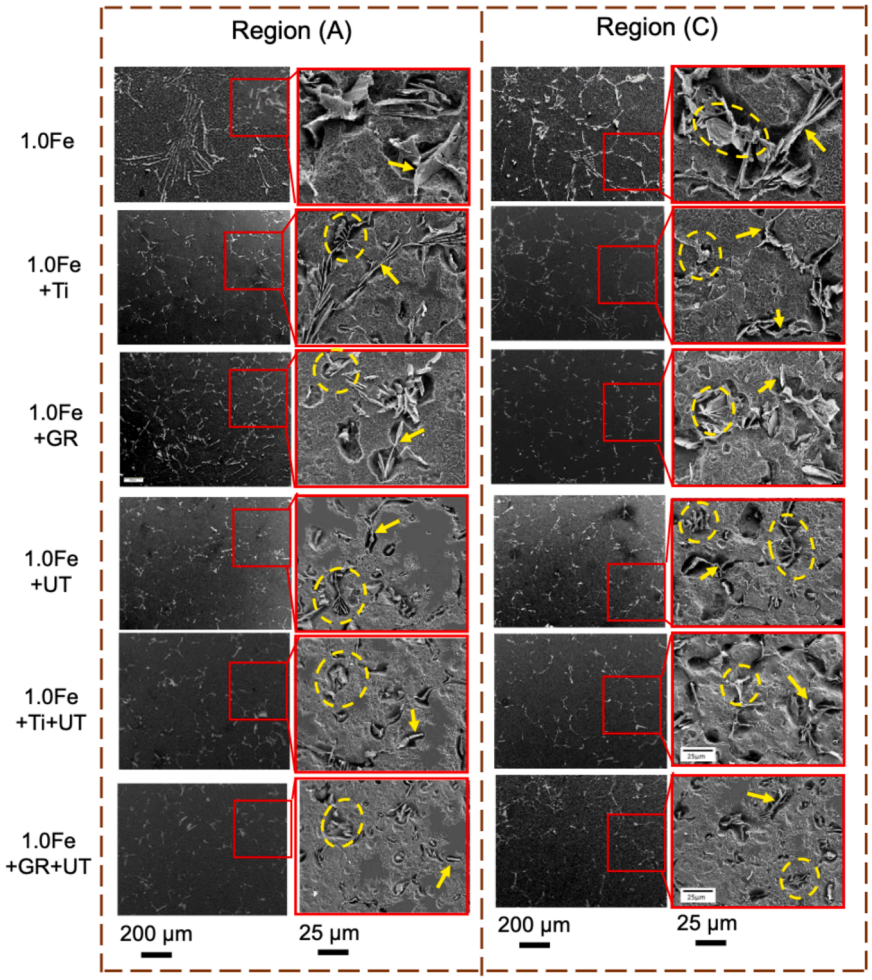

Fig. 5. SEM-BSD micrographs for alloys showing the $\alpha - Al_8Fe_2Si$ (indicated by circle) and $\beta - Al_9Fe_2Si_2$ (indicated by arrow) IMC distribution at grain boundaries in the top 'A' and the bottom 'C' regions of the ingots.

Fe-IMCs near the radiator leading to an increase in their area fraction on the Al-matrix, as opposed to areas furthest from the radiator (region 'C') where the Fe-IMCs were larger. The highest area fraction was reported for alloy 1.0Fe+GR+UT, where the effect of UT combined with TiB_2 inoculation significantly increased Fe-IMC nucleation and dispersion inside the Al-matrix as shown in Fig. 5.

3.4. Thermodynamic prediction for the Fe-IMC formation

Thermodynamic predictions for the formation of different phases under equilibrium conditions are presented in Fig. 7(a) for the 1.0Fe and 1.0Fe+Ti alloys. The inoculated alloy 1.0Fe+GR was ignored as the Thermo-Calc software used in this work did not contain TiB_2 compound in its thermodynamic database for Al-alloys. The calculations show slight changes, mainly in the temperature ranges for phase formation, upon the addition of Ti solute when compared with the reference alloy. Fig. 7(a) indicates that the predominant phases predicted to from are primary-Al, $\alpha - Al_8Fe_2Si$ and $\beta - Al_9Fe_2Si_2$, with minor changes in the phase content between alloys 1.0Fe and 1.0Fe+Ti. Moreover, no Al-Ti or Fe-Ti phases are predicted to form. The solidification sequence for the reference alloy 1.0Fe suggests primary-Al nucleates first at 645 °C followed by the formation of $Al_{13}Fe_4$ at 636 °C. $Al_{13}Fe_4$ dissolves to nucleate $\alpha - Al_8Fe_2Si$ starting at 618 °C and formation of $\beta - Al_9Fe_2Si_2$ initiates at 594 °C. For the 1.0Fe+Ti alloy, the nucleation temperatures slightly differ from the reference alloy with primary-Al, $Al_{13}Fe_4$, $\alpha - Al_8Fe_2Si$; and $\beta - Al_9Fe_2Si_2$ starting to form at 647 °C, 638 °C, 616 °C and 596 °C, respectively. Since no $Al_{13}Fe_4$ IMC was observed in any of the samples, it is presumed that this phase perhaps forms as a precursor to $\alpha - Al_8Fe_2Si$ nucleation.

Fig. 7(b) presents the DSC traces recording the solidification events

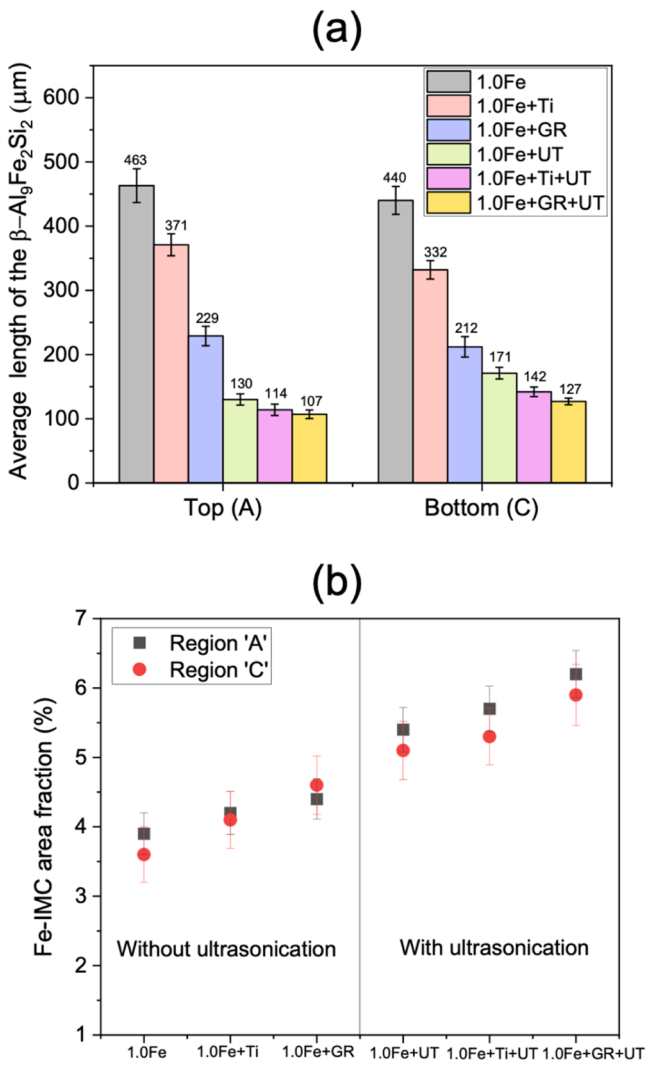

Fig. 6. (a) The calculated average length of the $\beta - Al_9Fe_2Si_2$ IMC in the top 'A' and bottom 'C' region of the alloy ingots and (b) the calculated area fraction for all Fe-IMCs in the alloy ingots.

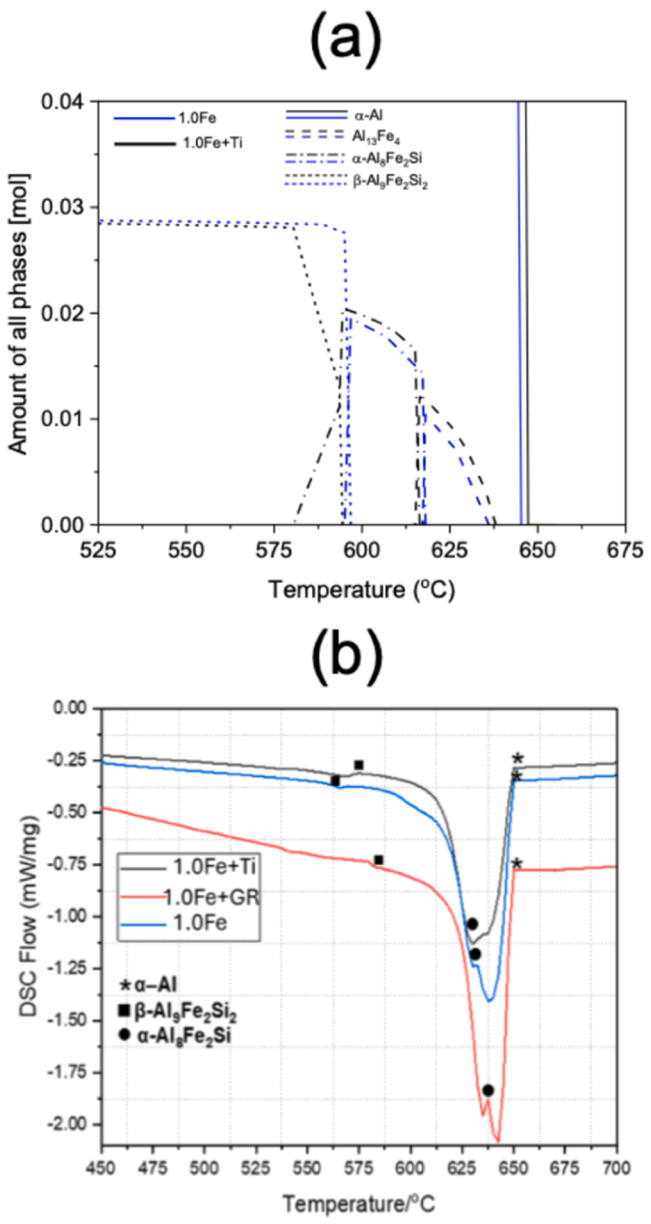

Fig. 7. (a) Thermo-Calc predicted solidification sequence for alloys 1.0Fe and 1.0Fe+Ti, note that only part of the Al solid fraction shown for clarity; (b) DSC traces for alloys 1.0Fe, 1.0Fe+Ti, 1.0Fe+GR during cooling from 700 °C.

for the 1.0Fe, 1.0Fe+Ti and 1.0Fe+GR alloys. Based on the DSC results and the observed microstructures, the main phases to form in these alloys are primary-Al, $\alpha - Al_8Fe_2Si$ and $\beta - Al_9Fe_2Si_2$. For the reference alloy 1.0Fe, the phase nucleation temperatures determined through DSC are 650 °C for primary-Al, 633 °C for $\alpha - Al_8Fe_2Si$ and 572 °C for $\beta - Al_9Fe_2Si_2$. Addition of solute Ti in the 1.0Fe+Ti alloy results in nucleation temperature to 650 °C for primary-Al, 634 °C for $\alpha - Al_8Fe_2Si$ and 576 °C for $\beta - Al_9Fe_2Si_2$. For the inoculated alloy 1.0Fe+GR, the nucleation temperatures recorded are 650 °C for primary-Al, 635 °C for $\alpha - Al_8Fe_2Si$; and 585 °C for $\beta - Al_9Fe_2Si_2$. The phase nucleation temperatures recorded through DSC are summarised in Table 2 and compared against the cooling curve measurements and Thermo-Calc predictions.

The phase nucleation temperatures determined through various techniques reasonably agree. There are minor differences that could be linked to the inherent nature of the techniques and samples used. For example, the primary-Al nucleation temperatures as determined though DSC doesn't indicate the enhanced nucleation effects from solute Ti and grain refiner. Considering the limited sample volume examined through DSC (20 mg) this is not surprising as there could be limited availability of TiB_2 nucleant or solute Ti for constitutional undercooling in the sample. Cooling curve measurement provides a better representation for Al-nucleation and shows excellent agreement with Thermo-Calc predictions, also demonstrating nucleation enhancement under solute Ti or Al-5Ti-1B inoculation. The Fe-IMC nucleation temperatures, as determined through DSC and Thermo-Calc prediction, show more noticeable difference though the trend observed are similar. It should be noted that equilibrium solidification simulation is used in the Thermo-Calc prediction while the actual solidification of the IMCs is most likely to follow non-equilibrium conditions. Despite this, the $Al_{13}Fe_4$ nucleation temperature predicted by Thermo-Calc shows good agreement with the $\alpha - Al_8Fe_2Si$ nucleation temperature determined through DSC. As stated earlier, $Al_{13}Fe_4$ being metastable and a precursor to $\alpha - Al_8Fe_2Si$ formation from Thermo-Calc predictions and the fact that final microstructure does not contain any $Al_{13}Fe_4$ phase, the first IMC peak noted in the DSC have been assigned to $\alpha - Al_8Fe_2Si$. Even if $Al_{13}Fe_4$ actually forms during solidification, its transformation to $\alpha - Al_8Fe_2Si$ does not produce detectable thermal effects in the DSC traces to separate them. An investigation arresting solidification or *in-situ* XRD measurements during solidification could clarify if $Al_{13}Fe_4$ forms during

solidification of the alloy. Nevertheless, the nucleation of $Al_{13}Fe_4$ (Thermo-Calc) and $\alpha - Al_8Fe_2Si$ (DSC) has been considered equivalent due to the reasons stated above. The larger difference in the nucleation temperature of $\beta - Al_9Fe_2Si_2$ measured through DSC and predicted by Thermo-Calc is presumable due to the strong non-equilibrium effects during the final stages of solidification.

3.5. Fe-IMC identification using EBSD analysis

EBSD were conducted to identify the crystal structures of Fe-IMCs and Fig. 8 displays the various EBSD maps acquired across all six ingots. Formation of the $\alpha - Al_8Fe_2Si$ and $\beta - Al_9Fe_2Si_2$ phases was verified using thermodynamic predictions and thermal analysis (DSC) and the EBSD results corroborate their presence in the microstructure. For all the alloy samples, the predominant Fe-IMCs were hexagonal $\alpha - Al_8Fe_2Si$ and monoclinic $\beta - Al_9Fe_2Si_2$. The chemical additions of Ti and GR or the physical employment of UT, as well as using both in conjunction, did not modify the Fe-IMC crystal structure or resulted in a different Fe-IMC phase. The $\alpha - Al_8Fe_2Si$ phase in this study was identified as $\alpha - Al_{7.04}Fe_{1.52}Si$ phase exhibiting hexagonal crystal structure with space group $P6_3/mmc$ with lattice parameters of $a = 1.24$ nm and $c = 2.62$ nm (ICSD 12931). The $\beta - Al_9Fe_2Si_2$ was indexed as $\beta - Al_9Fe_2Si_{1.5}$ (ICSD 74569) with a space group A_2/a with lattice parameters of $a = 0.626$ nm, $b = 0.6175$ nm, $c = 2.0813$ nm and $\beta - 90.42(3)^\circ$.

3.6. EDS analysis of elemental distribution

The EDS area scans, presented in Fig. 9(a-b), were conducted in regions 'A' and 'C' for the two TiB_2 inoculated alloys (1.0Fe+GR and 1.0Fe+GR+UT) to analyse the chemical composition in the intergranular region. Alloys 1.0Fe+Ti and 1.0Fe+Ti+UT, were also analysed using EDS, however, the low 0.03 wt%Ti addition in these alloys didn't provide any further insight and are not discussed here. The EDS maps for the two inoculated alloys (Fig. 9) revealed the presence of Fe, Si and Mg solute concentrations predominantly within the intergranular regions. This confirmed the Fe-IMC development in the solute rich liquid films around the primary-Al grains [12,24,25] as also predicted by Thermo-Calc and DSC of their formation following primary-Al solidification. Presence of Mg in the in these areas could also suggest formation of small amount of Mg_2Si.

The EDS analysis confirmed residual TiB_2 particles being present in the inter granular regions between primary-Al grains for both inoculated alloys. Fig. 9(a-b) shows the presence of Ti based particles visible as bright green spots, but B was faintly detectable in the area scan due to low concentration, However, spot scan confirmed the presence of B peak associated with these particles. For the inoculated alloys, a total of 10 elemental maps were collected from each alloy and the Ti concentration was averaged out from the regions 'A' and 'C'. For alloy 1.0Fe+GR, there is minor difference in the Ti concentration between region 'A' (7.3 ± 0.06 wt%) and region 'C' (7.5 ± 0.07 wt%). For the 1.0Fe+GR+UT alloy, a more noticeable difference in Ti concentration was recorded between region 'A' (7.8 ± 0.07 wt%) and 'C' (6.1 ± 0.08 wt%). Based on the results, the difference in Ti concentrations between the different regions of the alloys is attributed to the effects of ultrasonication on the distribution of the TiB_2 particles during solidification.

To identify any link between the TiB_2 particles and the growth of the Fe-IMCs, chemical analysis of the Fe-IMC areas was conducted for alloys 1.0Fe+GR and 1.0Fe+UT+GR, using SEM-EDS as shown in Fig. 10 (a-b). The high-resolution SEM images and corresponding EDS analysis revealed TiB_2 particles embedded at the centre of the $\alpha - Al_8Fe_2Si$ particles. In Fig. 10, the IMCs appear to grow outwards from the centre, resembling a flower like structure. The EDS analysis showed TiB_2 particles located inside the flower-shaped structure of $\alpha - Al_8Fe_2Si$ phase with more TiB_2 particles clustered in the non-sonicated sample. Notably, while these particles were absent in the $\beta - Al_9Fe_2Si_2$ phase, they were

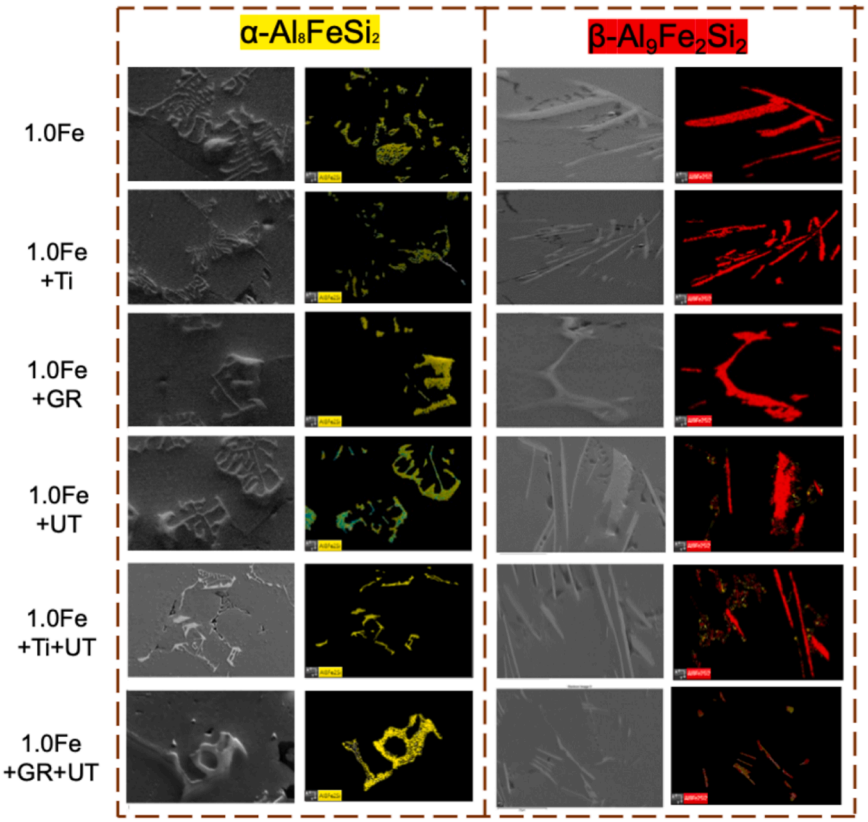

Fig. 8. EBSD micrographs showing phase maps for the $\alpha - Al_8Fe_2Si$ and $\beta - Al_9Fe_2Si_2$ IMC for all alloys.

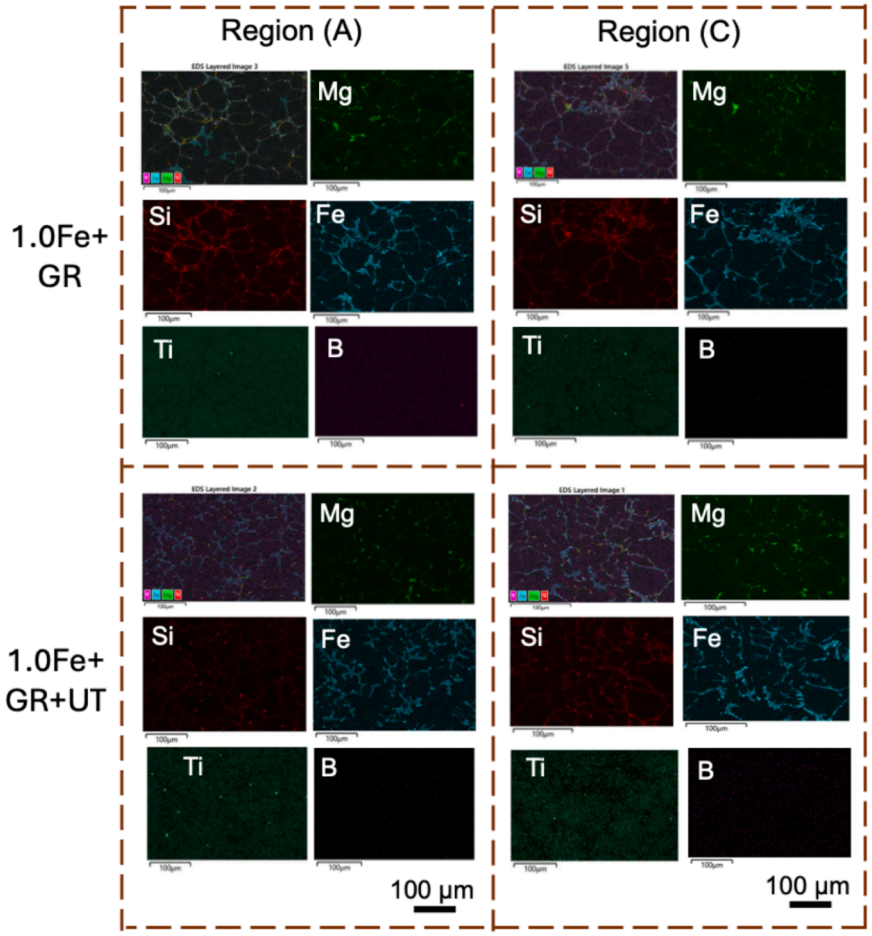

Fig. 9. EDS maps showing different elemental distributions across samples 1.0Fe+GR and 1.0Fe+GR+UT.

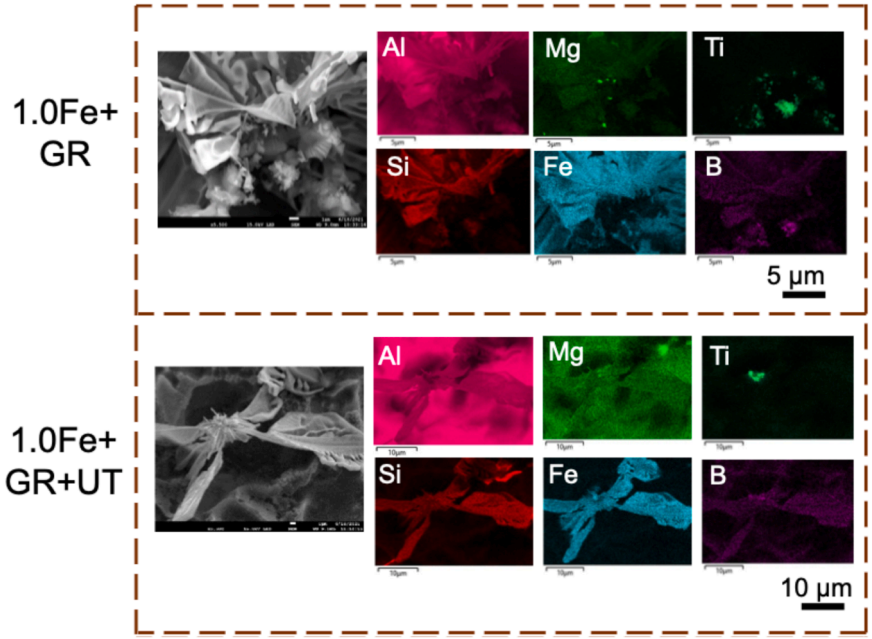

Fig. 10. EDS maps showing solute distribution within TiB_2 particles on the eutectic $\alpha - Al_8Fe_2Si$ phase in (a) 1.0Fe+GR and (b) 1.0Fe+GR+UT'.

present within the $\alpha - Al_8Fe_2Si$ phase. The SEM images in Fig. 11 show the 3-dimensional morphology of the $\alpha - Al_8Fe_2Si$ IMC phase in deep etched 1.0Fe+GR and 1.0Fe+GR+UT alloy samples. The $\alpha - Al_8Fe_2Si$ IMC phase exhibits both skeletal and petal like structures with TiB_2 particle clusters embedded in them suggesting TiB_2 may have played a role in their nucleation.

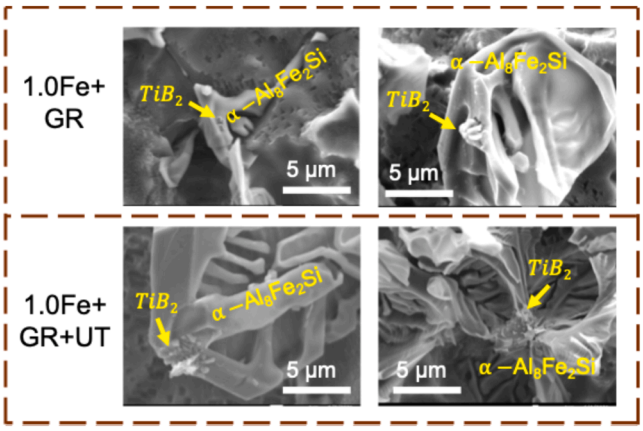

Fig. 11. SEM images from deep-etched 1.0Fe+GR and 1.0Fe+GR+UT showing the 3-dimensional morphology of the $\alpha - Al_8Fe_2Si$ phase with TiB_2 particles embedded within.

4. Discussion

4.1. Refinement of primary-Al grains

Figs. 2 and 3 clearly indicates that addition of solute Ti led to a drastic reduction in the primary-Al grain size of the reference 1.0Fe alloy. A corresponding increase in the primary-Al nucleation temperature in the cooling curves (Fig. 4) suggests nucleation enhancement. Typically, Ti solute concentration above 0.15 wt%, leads to Al_3Ti phase formation that act as effective heterogeneous nucleant for primary-Al grains due to excellent crystallographic matching. However, according to the Al-Ti phase diagram presented in Fig. 12, no Al_3Ti phase is expected in the current alloy with 0.03 wt% Ti [26]. No Al_3Ti formation was also predicted through Thermo-Calc simulation and none observed in the microstructure (although Al_3Ti is expected to dissolve through peritectic reaction during Al grain nucleation. It was suggested in the studies by Refs. [27–29] that lower Ti (less than 0.15 wt%) has a solute effect on primary-Al microstructures, as Ti has a comparatively high partition coefficient of 7.8, allowing grain refinement via growth restriction [10].

On the other hand, better refinement of the Al grain structure observed in the inoculated 1.0Fe+GR sample compared to 1.0Fe+Ti is expected as the high efficiency of TiB_2 particles in nucleating Al-grains is well-established. This is also corroborated by further increase in the primary-Al nucleation temperature in the cooling curves. It was noted that, for the alloys without ultrasonication, the grain size progressively increased from the bottom (Region 'C') to the top (Region 'A') of the ingots. This is expected since the solidification rate and the dissipation of heat is fastest around the mould wall and the bottom of the mould during casting [9]. The faster cooling also accentuates the development of constitutional supercooling in the Ti added sample and settling of some TiB_2 clusters is also expected towards the bottom of the mould, leading to the finest Al grain structures observed in this area.

The most significant Al grain refinement was observed in the samples with UT. Application of UT to the reference alloy (1.0Fe+UT) produced better Al grain refinement than even the chemically inoculated 1.0Fe+GR alloy ingots (Fig. 2). Moreover, grain refinement was observed throughout the ingots along with lower variation in the grain

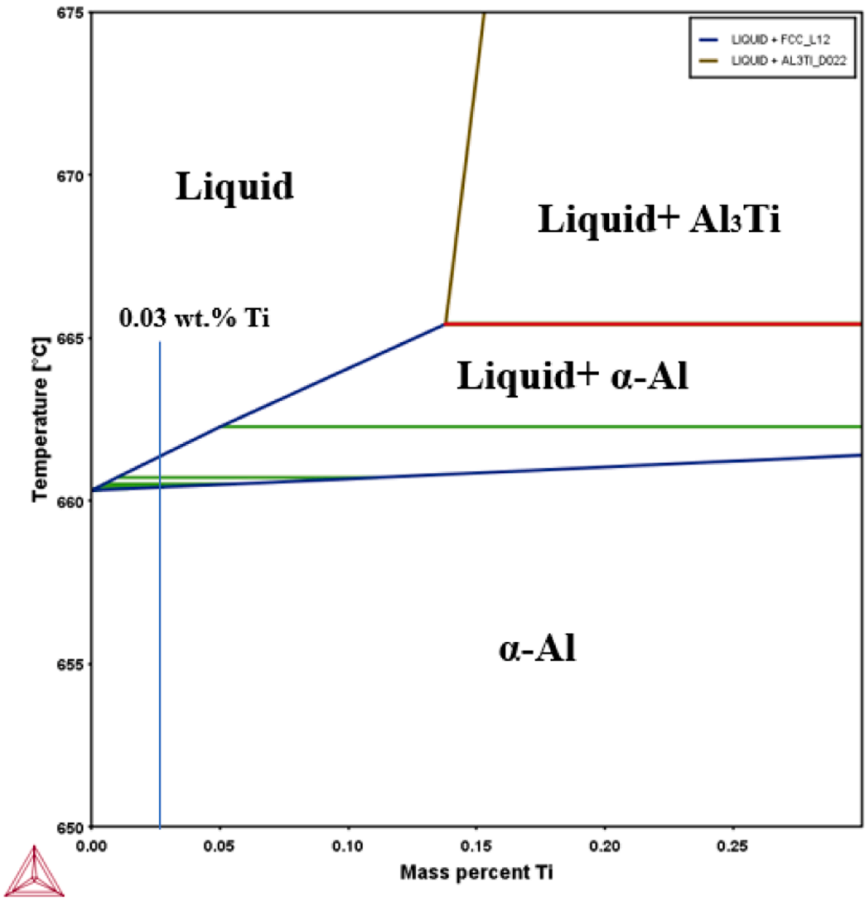

Fig. 12. Thermo-Calc prediction of the Al-rich corner of the Al-Ti phase diagram showing the phase formation during solidification. Note that Al_3Ti does not form in the present alloy with 0.03 %Ti addition.

size between the top and the bottom regions of the ingots (Fig. 3). However, in contrast the chemical routes, UT treated samples showed an increase in the Al grain size from the top towards the bottom of the ingots. Ultrasound effect on the solidification microstructure evolution is predominantly explained on the basis of cavitation. Hence the grain refinement is most prominent at the top of the ingot near the radiator where cavitation is prevalent [2,4,8]. The primary-Al grain refinement observed in the rest of the ingots is likely contributed by acoustic streaming effect (even in the absence of intense cavitation further away from the horn) that disperses dendrite fragments and nuclei throughout the melt [4,7,8]. In addition, the reduced recalescence observed under UT in the cooling curves (Fig. 4) may indicate better dispersion of the latent heat from the solid-liquid interface, thereby prolonging nucleation and better dispersal of nuclei through acoustic streaming effects. All the UT samples also showed consistently higher nucleation temperature for primary-Al in the cooling curves suggesting cavitation enhanced heterogeneous nucleation in these samples [4]. While the addition of Ti or GR with UT only showed marginally better grain refinement compared to ultrasonication alone, the grain size appears to be more uniform throughout the ingot with the finest grains and best microstructural uniformity observed in the 1.0Fe+GR+UT sample. TiB_2 particles are expected to cluster and then start settling towards the bottom of the ingot during solidification aiding the finer Al-grain formation at the base of the 1.0Fe+GR ingot as shown schematically in Fig. 13. Cavitation under UT prevents the TiB_2 clustering and distributes them throughout the ingot against any gravitational settling. Similar observation has been made in the work by Ref. [30,31], where UT prevented aggregation of suspended nano-particles. This allows UT to further enhances the grain refining capability of TiB_2 particles in the entire volume of liquid as shown schematically in Fig. 13. More TiB_2 particles are available at the top of the 1.0Fe+GR+UT ingot to nucleate Al grain. Along with the presence of cavitation, this leads to the finest grain structure at the top and the finest overall grain structure with minimal variation throughout the ingot.

4.2. Fe-IMC evolution at the solid/liquid (S/L) interface

The effect of Ti and TiB_2 on Fe-IMC formation was studied using Thermo-Calc predictions and DSC analysis as shown in Fig. 7. Thermo-Calc simulation indicates only minor changes to $\alpha - Al_8Fe_2Si$ and $\beta - Al_9Fe_2Si_2$ phase content and nucleation temperatures (further confirmed through DSC measurements) from the addition of Ti. This suggests solute Ti does not significantly influence the nucleation behaviour of IMCs (see Table 2). The minor increase in the IMC nucleation temperatures under Ti solute addition could be related to refinement of primary-Al grains, which is in agreement with the reported work by Ref. [12]. It was mentioned in their work that grain refinement may potentially increase nucleation of Fe-IMCs due to changes in the elemental segregation at the Al-grain boundaries, this in turn influencing Fe-IMC nucleation. Table 2 also indicates that $\alpha - Al_8Fe_2Si$ and$\beta - Al_9Fe_2Si_2$ nucleate at slightly higher temperatures under inoculation as determined through DSC. While the increase in the nucleation temperature for $\alpha - Al_8Fe_2Si$is not significant, the DSC traces (Fig. 7b) show a more prominent thermal peak corresponding to the nucleation of $\alpha - Al_8Fe_2Si$ with GR addition. This could be attributed to the residual TiB_2 particles segregated in the intergranular liquid channels helping heterogeneous nucleation of Fe-IMCs, as observed in Fig. 10 (a-b). Similar observation has also been made in our previous investigation [2].

It is known that Fe and Si segregates at the grain boundaries during the solidification process due to their low solubility in Al. As the concentration of Fe at the S/L interface exceeds its solubility limit, Fe-IMCs ($\alpha - Al_8Fe_2Si$ and$\beta - Al_9Fe_2Si_2$) nucleate [32–34]. Earlier studies found that primary-Al grain shape and size influence Fe and Si segregation at the S/L interface [20,35–40]. In the presence of primary-Al, Fe and Si could accumulate preferentially in certain regions promoting the nucleation of specific Fe-IMC phases over the others [20,30]. Moreover, for the inoculated alloy, the presence of TiB_2 particles may help $\alpha - Al_8Fe_2Si$ nucleation as shown in Fig. 10. The DSC results (Fig. 7(b), Table 2) also indicate a noticeable increase in the $\beta - Al_9Fe_2Si_2$ nucleation temperature in the inoculated alloy although TiB_2 particles were predominantly observed within the $\alpha - Al_8Fe_2Si$ phase (Figs. 10 and 11). Studies by Refs. [8,41] found that TiB_2 {0001} basal plane exhibits a strong crystallographic matching with the $Al_{13}Fe_4$ phase. This may lead to TiB_2 particles nucleating the $Al_{13}Fe_4$ phase that transforms to stable $\alpha - Al_8Fe_2Si$and the $\beta - Al_9Fe_2Si_2$ nucleates off the 'earlier' $\alpha - Al_8Fe_2Si$ phase. This could explain why TiB_2 particles were embedded predominantly in the $\alpha - Al_8Fe_2Si$ phase, as it catalysed nucleation and

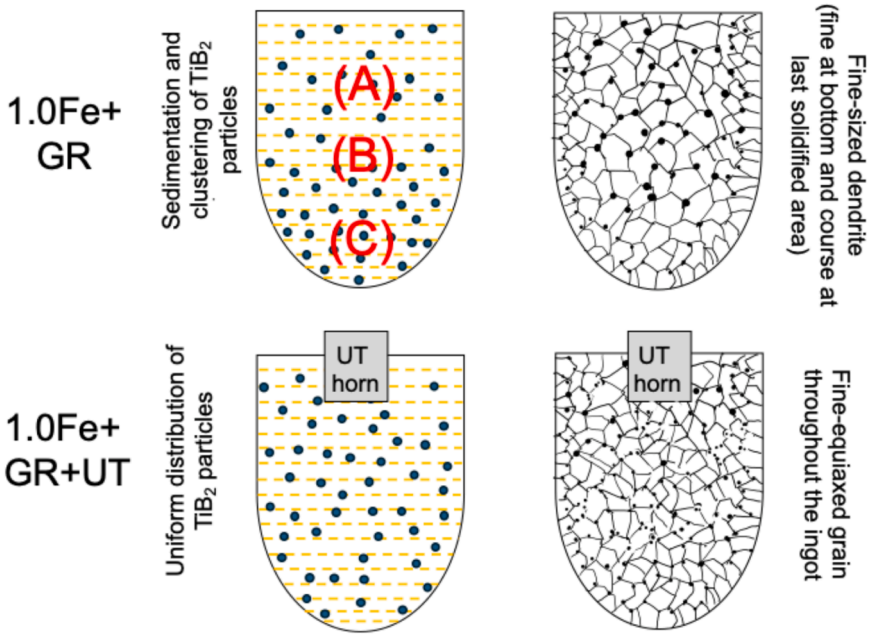

Fig. 13. Schematic representation of TiB_2 particle distribution in the melt (left) and Al-grain formation (right) for (a) 1.0Fe+GR and (b) 1.0Fe+GR+UT ingots. Note that UT prevents settling of TiB_2 clusters to the bottom of the melt promoting better dispersion near the top (region 'A'). Note that the figure is not drawn to scale.

formation of the first Fe-IMC phases. More α − Al_8Fe_2Si nucleation could potentially increase sites for subsequent β − $Al_9Fe_2Si_2$ nucleation leading to an increase in its nucleation temperature under inoculation.

It is hypothesised that after primary-Al nucleation, residual TiB_2 particle not involved in Al-grain formation will cluster in the remnant liquid pockets and get impinged by the growing primary-Al front. The diffusion of solutes (Fe/Si) catalyses heterogenous nucleation of first IMCs on the residual TiB_2 particles. The findings from Ref. [13] is in agreement with the results observed in this study. This is explained schematically in Fig. 14;

(a) Residual TiB_2 particles suspended in the liquid are "pushed" ahead of the S/L interface. The Fe and Si also diffuse into these liquid pockets.
(b) The impingement by the S/L interface causes the residual TiB_2 particles to also cluster.
(c) Heterogenous nucleation of IMCs at the S/L interface commences, initiating α − Al_8Fe_2Si growth.
(d) The α − Al_8Fe_2Si nucleates in the narrow liquid films at the S/L interface. The TiB_2 particles suspended in the liquid may catalyse some direct nucleation of the α − Al_8Fe_2Si or become engulfed onto the growing α − Al_8Fe_2Si phase.

4.3. Influence of primary-Al grain structure on the nucleation and growth of Fe-IMC within liquid pockets

It has been reported that the formation of α − Al_8Fe_2Si is followed by coupled growth of β − $Al_9Fe_2Si_2$ phase at the primary-Al grains [35,39,42,43]. Fig. 15 (a-f) schematically shows the effects of primary-Al grain structure on the intergranular liquid pockets and subsequent evolution of IMCs in them. In our previous work [2] it was suggested that coarse dendrites tend to have larger but more scattered residual liquid pockets with more 'space' for the growth of Fe-IMCs during solidification. Hence the Fe-IMCs forming between coarse dendritic grains tend to be thicker and longer but less likely to create an interconnected IMC network, as has been observed for the reference 1.0Fe alloy. It should be noted that the schematic (Fig. 15a), especially when coarse dendrite grains form, is an oversimplification of the mechanism where the interdendritic liquid pockets are expected to be even more confined.

However, this is not the case for 1.0Fe+Ti and 1.0Fe+GR samples exhibiting finer Al-grains. Smaller grains allow for small but well-distributed and interconnected intergranular liquid pockets leading to more Fe-IMC nucleation sites as the number of liquid pockets increase [39,44]. As a result, the Fe-IMCs in these alloys are smaller in size but also form a more interconnected network through the sample. This also increases their area fraction as observed in the present investigation.

UT significantly refines the Al-grain structure and produces non-dendritic grains. Consequently, the residual liquid pockets are drastically smaller and the Fe-IMCs evolving in these samples are finer and better distributed as shown in Fig. 5. The combined effect of UT and TiB_2 for alloy 1.0Fe+GR+UT resulted in the finest and most uniform primary-Al grain structure, and subsequently, resulted in the finest Fe-IMCs with highest area faction (Fig. 6) of all samples for reasons stated above.

4.4. The Role of GR and UT on Fe-IMC evolution

The previous section explains the role played by primary-Al grain structure on the evolution of Fe-IMCs. Even though the results from this investigation suggest TiB_2 may help nucleating α − Al_8Fe_2Si(see Section 3.6 and Figs. 10, 11), IMC growth and size is dictated primarily by the size and distribution of remnant intergranular liquid pockets influenced by the existing Al-grain structure. This is primarily due to the IMCs solidifying last in the intergranular eutectic areas in the present alloys. On the contrary, GR may play a direct and dominant role in IMC nucleation and growth (size and distribution) where they form during the initial stages of solidification (say through peritectic reactions). Accordingly, in the present alloys, the role of GR on Fe-IMC evolution is indirect and comes predominantly through the refinement of Al-grain structure and intergranular liquid pockets.

Similarly, although all ultrasonicated samples demonstrated finer Fe-IMC structures compared to chemical treatment alone, Fe-IMC solidification had occurred outside the direct influence of ultrasonication. This is due to the radiator having been already withdrawn prior to Fe-IMC solidification or the Al solid fraction being high enough to negate reasonable ultrasound transmission to remnant liquid. The finer IMCs observed in the presence of UT can't be explained on the basis of

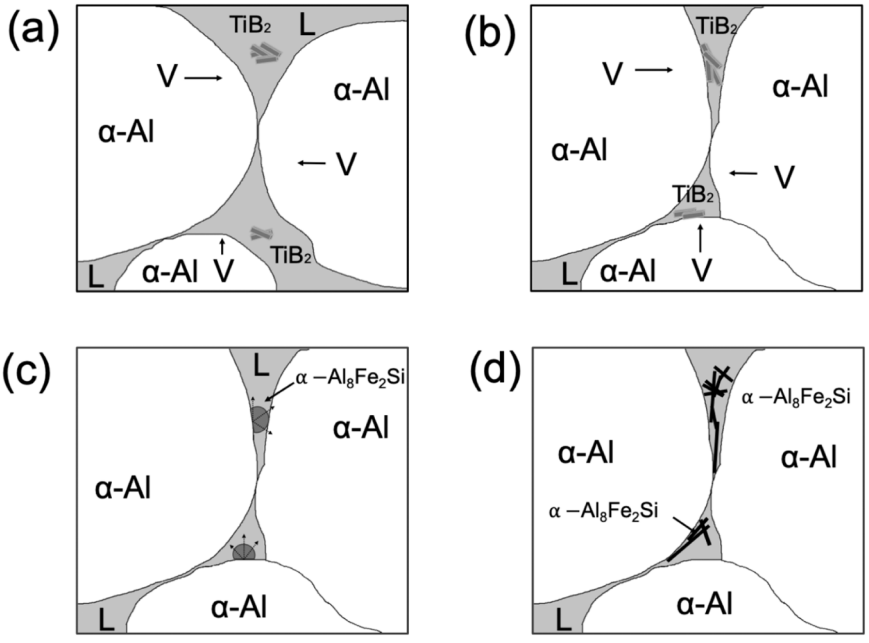

Fig. 14. Schematic representation of residual TiB_2 particle distribution and $\alpha - Al_8Fe_2Si$ nucleation in the intergranular regions: (a) residual TiB_2 particles segregate at the S/L interface; (b) primary-Al S/L interface impinging upon TiB_2 clusters and enrichment of the liquid with rejected Fe and Si; (c) heterogenous nucleation of $\alpha - Al_8Fe_2Si$ on available TiB_2 clusters; (d) Nucleation of $\alpha - Al_8Fe_2Si$ commences in the remaining liquid areas. Note that the figure is not drawn to scale.

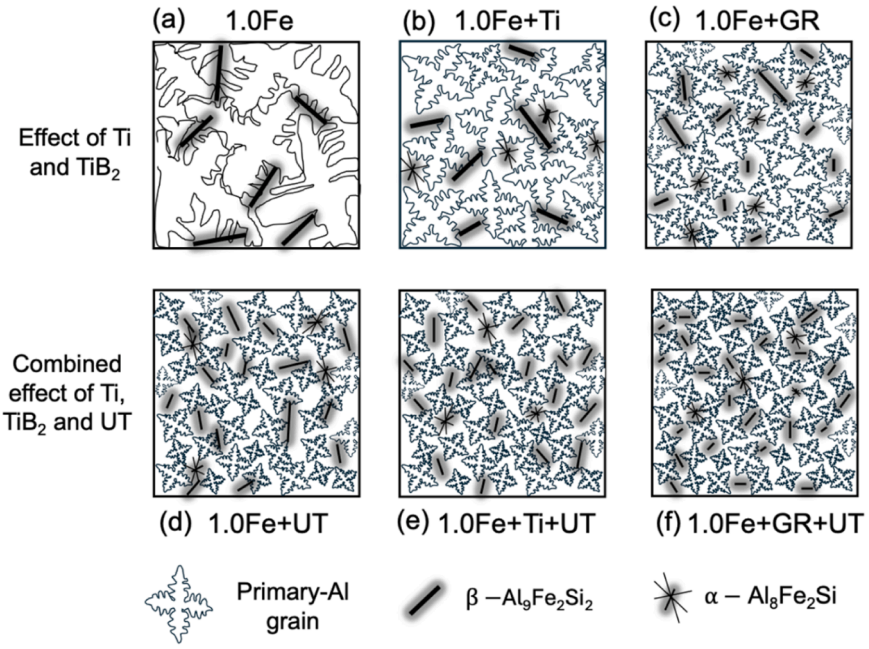

Fig. 15. Schematic illustration of Al grain formation and its effect on liquid pocket distribution and subsequent Fe-IMC formation (shown in red circles in (a) and (d)). for alloys; (a) 1.0Fe (b) 1.0Fe+Ti (c) 1.0Fe+GR (d) 1.0Fe+Ti+UT (e) 1.0Fe+Ti+UT and (f) 1.0Fe+GR+UT. Note that the figure is not drawn to scale.

cavitation induced nucleation, fragmentation or distribution of IMCs in the present alloys. As with the chemical routes, the finer IMCs are explained through the UT-enhanced grain refinement of primary-Al that leads to finest and well-dispersed liquid pockets for the IMCs to form and grow as explained in the previous section. The finer Al-grain structure observed under UT also translates into finer Fe-IMC structure in a direct correlation. Application of UT along with GR promotes better dispersion of TiB_2 particles, as explained in Section 4.1 and Fig. 13, indirectly enhancing the IMC nucleation through availability of unused TiB_2 particles (see Section 3.6) throughout the ingot. However, the size and distribution of Fe-IMCs is still primarily contributed by the existing Al-grain structure that is the finest in the alloy 1.0Fe+GR+UT.

5. Conclusions

In this research, a total of six Al-Mg-Si alloys with Fe content of 1.0 wt% were cast in graphite mould under similar solidification conditions. Al-5Ti-1B chemical grain refiner (GR) and solute Ti were added, with and without ultrasonication (UT), to assess their effects in primary-Al grain refinement and Fe-based intermetallic compound (Fe-IMC) evolution. Detailed examination through advanced microstructural characterizations and thermal analysis techniques were employed to analyse the role played by the solute, GR and UT on the microstructure development. The following conclusions were drawn from the results:

(1) The coarse dendritic primary-Al grain structure was refined with an increase in the Al nucleation temperature due to the constitutional undercooling effect from solute Ti addition. Further refinement in the Al grain structure and enhancement of its nucleation temperature was observed through GR addition instead of solute-Ti due to the effectiveness of TiB_2 particles in nucleating Al-grains. The grain size progressively increased from the bottom to the top of the ingots due to the reduction in cooling rate and settling of TiB_2.
(2) UT consistently produced finer non-dendritic Al grain structure throughout the ingots and further enhanced the refining effect of solute Ti or GR. UT in conjunction with GR produced better dispersion of TiB_2, especially at the top of the mould, leading to the finest and most uniform grain structure. Al nucleation temperature increased further with a reduction in recalescence under UT, compared to Ti or GR alone, indicating cavitation enhancing and prolonging nucleation. Under UT, grain size increased (although marginally) from the top to the bottom of the ingots as opposed to non-UT ingots due to decreasing cavitation with distance from the radiator at the top.
(3) $\alpha - Al_8Fe_2Si$ and $\beta - Al_9Fe_2Si_2$ IMCs nucleated consecutively following primary-Al solidification and were the predominant Fe-IMC phases present in all alloys. Addition of Ti and GR promoted refinement in the Fe-IMC size with better dispersion through the ingots. Although the increase in Fe-IMCs nucleation temperature is marginal with Ti or GR addition, observation of TiB_2 embedded at the centre of $\alpha - Al_8Fe_2Si$ suggests a role of residual GR particles in IMC nucleation.
(4) The finest and best distributed Fe-IMCs were observed in the UT ingots even though they formed outside the effective application regime of ultrasonication. UT in conjunction with Ti or GR addition further refined the Fe-IMC size over the chemical means alone replicating the effects observed with Al-grain refinement. The finest and most uniform Fe-IMCs were observed in the alloy with GR and UT along with better dispersion of residual TiB_2 in the intergranular areas.
(5) While the Al-grain refinement observed in the alloys directly resulted from the individual or combined application of chemical (solute-Ti, GR) or physical (UT) means, the refinement in the Fe-IMCs appears to be indirect and resulting as a consequence of Al-grain refinement. Despite the indication of residual TiB_2 segregation at the solid-liquid interface aiding Fe-IMC nucleation, the predominant contributor to the Fe-IMC growth and size appears to be the size and distribution of intergranular liquid pockets. Better Al-grain refinement contributed to finer Fe-IMCs due to refinement and dispersion of the intergranular liquid pockets where the IMCs formed.

Declaration of Competing Interest

The authors declare that they have no known competing financial interests or personal relationships that could have appeared to influence the work reported in this paper.

Acknowledgments

This research was funded by the Industrial Cooperative Awards in Science & Technology (CASE) (voucher no. 17000037). In addition to that, the characterisation facility is supported from the Higher Education Funding Council for England (HEFCE) fund and the WMG Centre for High Value Manufacturing Catapult is gratefully acknowledged.

Data availability

Data will be made available on request.

References

[1] J.E. Hatch, Aluminum Properties and Physical Metallurgy, American Society for Metals, Ohio, USA, 1984.
[2] M.H. Khan, A. Das, Z. Li, H.R. Kotadia, Effects of Fe, Mn, chemical grain refinement and cooling rate on the evolution of Fe intermetallics in a model 6082 Al-alloy, Intermetallics 132 (2021) 107132, https://doi.org/10.1016/j.intermet.2021.107132.
[3] Y. Zhou, "Solidification behaviour of Fe-rich intermetallic compounds in aluminium alloys," 2018, [Online]. Available: ⟨http://bura.brunel.ac.uk/handle/2438/15965⟩.
[4] S.G. Shabestari, The effect of iron and manganese on the formation of intermetallic compounds in aluminum-silicon alloys, Mater. Sci. Eng. A 383 (2) (2004) 289–298, https://doi.org/10.1016/j.msea.2004.06.022.
[5] S.G. Shabestari, M. Mahmudi, M. Emamy, J. Campbell, Effect of Mn and Sr on intermetallics in Fe-rich eutectic Al-Si alloy, Int. J. Cast. Met. Res. 15 (1) (2002) 17–24, https://doi.org/10.1080/13640461.2002.11819459.
[6] J. Ding, C. Wang, C. Lu, G. Zhu, N. Guo, X. Gao, X. Wang, Preparation of Al_3Ti-Al_2O_3/Al Inoculant and Its Inoculation Effect on Al-Cu-Mn Alloy, Materials 16 (15) (2023) 52–64.
[7] X. Dong, Y. Zhang, S. Ji, Enhancement of mechanical properties in high silicon gravity cast AlSi9Mg alloy refined by Al3Ti3B master alloy, Mater. Sci. Eng. A 700 (April) (2017) 291–300, https://doi.org/10.1016/j.msea.2017.06.005.
[8] Z. Fan, Y. Zhang, T. Qin, X.R. Zhou, G.E. Thompson, T. Pennycook, T. Hashimoto, Grain refining mechanism in the Al/Al-Ti-B system, Acta Mater. 84 (2015) 292–304, https://doi.org/10.1016/j.actamat.2014.10.055.
[9] H.R. Kotadia, M. Qian, A. Das, Solidification of aluminium alloys under ultrasonication: an overview, Trans. Indian Inst. Met. 71 (11) (2018) 2681–2686, https://doi.org/10.1007/s12666-018-1446-1.
[10] G.I. Eskin, Y.P. Pimenov, G.S. Makarov, Effect of cavitation melt treatment on the structure refinement and property improvement in cast and deformed hypereutectic Al-Si alloys, Mater. Sci. Forum 242 (1997) 65–70, https://doi.org/10.4028/www.scientific.net/msf.242.65.
[11] F. Wang, D. Eskin, T. Connolley, J. Mi, Effect of ultrasonic melt treatment on the refinement of primary Al3Ti intermetallic in an Al-0.4Ti alloy, J. Cryst. Growth 435 (December) (2016) 24–30, https://doi.org/10.1016/j.jcrysgro.2015.11.034.
[12] K.O. Verma, S. Kumar, P. Grant, Influence of cooling rate on the Fe intermetallic compound formation in an AA6063 Al alloy, J. Alloy. Compd. 555 (2013) 274–282.
[13] A. Lui, P.S. Grant, I.C. Stone, K.A.Q. O'Reilly, The role of grain refiner in the nucleation of alfesi intermetallic phases during solidification of a 6xxx aluminum alloy, Metall. Mater. Trans. A Phys. Metall. Mater. Sci. 50 (11) (Nov. 2019) 5242–5252, https://doi.org/10.1007/s11661-019-05447-y.
[14] H.R. Kotadia, Solidification behaviour of Al-Sn-Cu immiscible alloys and Al-Si cast alloys processed under intensive shearing, no. 2010, [Online]. Available: ⟨http://bura.brunel.ac.uk/handle/2438/4517⟩.
[15] H.R. Kotadia, E. Doernberg, J.B. Patel, Z. Fan, R. Schmid-Fetzer, Solidification of Al-Sn-Cu based immiscible alloys under intense shearing, Metall. Mater. Trans. A Phys. Metall. Mater. Sci. 40 (9) (2009) 2202–2211, https://doi.org/10.1007/s11661-009-9918-x.
[16] J.A. Morton, D.G. Eskin, N. Grobert, J. Mi, K. Porfyrakis, K. Prentice, I. Tzanakis, Effect of temperature and acoustic pressure during ultrasound liquid-phase processing of graphite in water, Jom (2021), https://doi.org/10.1007/s11837-021-04910-9.
[17] F. Jiang, K. qiang Qiu, H. ding Wang, Q. chun Xiang, Y. ran Zhang, Y. dong Qu, Effects of Bi modification and ultrasonic treatment on microstructure evolution and mechanical properties of AlMg5Si2Mn alloy, J. Alloy. Compd. 901 (2022) 163486, https://doi.org/10.1016/j.jallcom.2021.163486.
[18] H.R. Kotadia, A. Das, E. Doernberg, R. Schmid-Fetzer, A comparative study of ternary Al-Sn-Cu immiscible alloys prepared by conventional casting and casting under high-intensity ultrasonic irradiation, Mater. Chem. Phys. 131 (1–2) (2011) 241–249, https://doi.org/10.1016/j.matchemphys.2011.09.020.
[19] X. Zhang, H.R. Kotadia, J. Depner, M. Qian, A. Das, Effect of ultrasonication on the solidification microstructure in al and mg-alloys, Miner. Met. Mater. Ser. (January) (2019) 1589–1595, https://doi.org/10.1007/978-3-030-05864-7_201.
[20] H.R. Kotadia, N. Hari Babu, H. Zhang, S. Arumuganathar, Z. Fan, Solidification behavior of intensively sheared hypoeutectic Al-Si alloy liquid, Metall. Mater. Trans. A Phys. Metall. Mater. Sci. 42 (4) (2011) 1117–1126, https://doi.org/10.1007/s11661-010-0516-8.
[21] D.G. Eskin, J. Zuidema, V.I. Savran, L. Katgerman, Structure formation and macrosegregation under different process conditions during DC casting, Mater. Sci. Eng. A 384 (1–2) (2004) 232–244, https://doi.org/10.1016/j.msea.2004.05.066.
[22] G.I. Eskin, Broad prospects for commercial application of the ultrasonic (cavitation) melt treatment of light alloys, Ultrason. Sonochem. 8 (3) (2001) 319–325, https://doi.org/10.1016/S1350-4177(00)00074-2.
[23] C.J. Todaro, Refinement of the Microstructure of Light Alloys using Ultrasonic and Laser Processing, PhD thesis, 2019.
[24] F. Wang, Z. Liu, D. Qiu, J.A. Taylor, M.A. Easton, M.X. Zhang, Revisiting the role of peritectics in grain refinement of Al alloys, Acta Mater. 61 (1) (2013) 360–370, https://doi.org/10.1016/j.actamat.2012.09.075.
[25] Y. Zhou, Solidification Behaviour of Fe - Rich Intermetallic Compounds in Aluminium Alloys," PhD thesis, Brunel University, London, 2018.
[26] S. Carlsson, Grain refinement of aluminium by titanium diboride particles The importance of nucleation, growth restriction, and cooling rate, MSc Thesis, K. Tek. H. ögskolan (2019) 1–50.
[27] K. Kashyap, T. Chandrashekar, Asia/Pacific Big Data and Cognitive/Artificial Intelligence Systems and Content Analytics, Bull. Mater. Sci. 24 (4) (2001) 345–353.
[28] J.A. Spittle, S. Sadli, Effect of alloy variables on grain refinement of binary aluminium alloys with Al–Ti–B, Mater. Sci. Technol. 11 (6) (1995) 533–537.
[29] X.B. Qi, Y. Chen, X.H. Kang, D.Z. Li, Q. Du, An analytical approach for predicting as-cast grain size of inoculated aluminum alloys, Acta Mater. 99 (2015) 337–346, https://doi.org/10.1016/j.actamat.2015.08.006.
[30] M. Sandhya, D. Ramasamy, K. Sudhakar, K. Kadirgama, W.S.W. Harun, Ultrasonication an intensifying tool for preparation of stable nanofluids and study the time influence on distinct properties of graphene nanofluids – a systematic overview, Ultrason. Sonochem. 73 (2021) 105479, https://doi.org/10.1016/j.ultsonch.2021.105479.
[31] A.P. Khrustalyov, A.A. Kozulin, I.A. Khmeleva, M.G. Vorozhstov, A.B. Eskin, S. Chankitmunkong, V.V. Platov, S.V. Vasilyev, Influence of titanium diboride particle size on structure and mechanical properties of an Al-Mg alloy, Metal (Basel) 9 (10) (2019), https://doi.org/10.3390/met9101030.
[32] T. Young, R. Clyne, An Al-Fe intermetallic compound phase formed during controlled solidifciation, Scr. Metall. 15 (11) (1981) 1211–1216.
[33] M. Karlík, T. Mánik, H. Lauschmann, Influence of Si and Fe on the distribution of intermetallic compounds in twin-roll cast Al-Mn-Zr alloys, J. Alloy. Compd. 515 (2012) 108–113, https://doi.org/10.1016/j.jallcom.2011.11.101.
[34] W. Yang, S. Ji, X. Zhou, I. Stone, G. Scamans, G.E. Thompson, Z. Fan, Heterogeneous nucleation of α-Al grain on primary α-AlFeMnSi intermetallic investigated using 3d sem ultramicrotomy and HRTEM, Metall. Mater. Trans. A 45 (9) (2014) 3971–3980, https://doi.org/10.1007/s11661-014-2346-6.
[35] C. Puncreobutr, A.B. Phillion, J.L. Fife, P. Rockett, A.P. Horsfield, P.D. Lee, In situ quantification of the nucleation and growth of Fe-rich intermetallics during Al alloy solidification, Acta Mater. 79 (2014) 292–303, https://doi.org/10.1016/j.actamat.2014.07.018.
[36] S. Henry, T. Minghetti, M. Rappaz, Dendrite growth morphologies in aluminium alloys, Acta Mater. 46 (18) (1998) 6431–6443, https://doi.org/10.1016/S1359-6454(98)00308-5.
[37] Y. Osawa, S. Takamori, T. Kimura, K. Minagawa, H. Kakisawa, Morphology of intermetallic compounds in Al-Si-Fe alloy and its control by ultrasonic vibration, Mater. Trans. 48 (9) (2007) 2467–2475, https://doi.org/10.2320/matertrans.F-MRA2007874.
[38] Y. Han, C. Ban, H. Zhang, H. Nagaumi, Q. Ba, J. Cui, Investigations on the solidification behavior of Al-Fe-Si alloy in an alternating magnetic field, Mater. Trans. 47 (8) (2006) 2092–2098, https://doi.org/10.2320/matertrans.47.2092.
[39] S. Kumar, K.A.Q. O'Reilly, Influence of Al grain structure on Fe bearing intermetallics during DC casting of an Al-Mg-Si alloy, Mater. Charact. 120 (2016) 311–322, https://doi.org/10.1016/j.matchar.2016.09.017.
[40] R.K. Koju, Y. Mishin, The role of grain boundary diffusion in the solute drag effect, Nanomaterials 11 (9) (2021), https://doi.org/10.3390/nano11092348.
[41] D. Wearing, A.P. Horsfield, W. Xu, P.D. Lee, Which wets TiB_2 inoculant particles: Al or Al3Ti? J. Alloy. Compd. 664 (2016) 460–468, https://doi.org/10.1016/j.jallcom.2015.12.203.
[42] Z. Que, Y. Wang, Z. Fan, Formation of the Fe-containing intermetallic compounds during Solidification of Al-5Mg-2Si-0.7Mn-1.1Fe Alloy, Metall. Mater. Trans. A 49 (6) (Jun. 2018) 2173–2181, https://doi.org/10.1007/s11661-018-4591-6.
[43] J. Mathew, G. Remy, M.A. Williams, F. Tang, P. Srirangam, Effect of Fe Intermetallics on Microstructure and Properties of Al-7Si Alloys, Jom 71 (12) (2019) 4362–4369, https://doi.org/10.1007/s11837-019-03444-5.
[44] S. Kumar, P.S. Grant, K.A.Q. O'Reilly, Evolution of Fe bearing intermetallics during DC casting and homogenization of an Al-Mg-Si Al alloy, Metall. Mater. Trans. A 47 (6) (2016) 3000–3014, https://doi.org/10.1007/s11661-016-3451-5.